Dalton Transactions

Accepted Manuscript

ROYAL SOCIETY OF CHEMISTRY

www.rsc.org/dalton

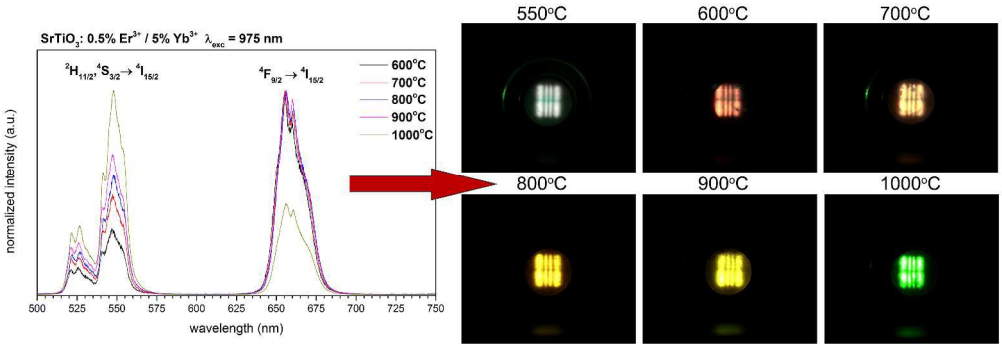

2469x848mm (72 x 72 DPI)

Functional up-converting $SrTiO_3:Er^{3+}/Yb^{3+}$ nanoparticles, structural features, particle size colour tuning and *in vitro* RBC cytotoxicity

R. Pazik [1*], **M. Mączka[1]**, M. Malecka[1], L. Marciniak[1], A. Ekner-Grzyb[2], L. Mrowczynska[3], and R.J. Wiglusz[1]

[1]*Institute of Low Temperature and Structure Research, PAS, Okólna 2, 50-422 Wrocław, Poland*

[2]*Adam Mickiewicz University, Faculty of Biology, Department of Behavioural Ecology, Umultowska 89, 61-614 Poznań, Poland*

[3]*A dam Mickiewicz University, Faculty of Biology, Department of Cell Biology, Umultowska 89, 61-614 Poznań, Poland*

[*]Corresponding author:
R.Pazik@int.pan.wroc.pl

Abstract

$SrTiO_3$ nanoparticles co-doped with a broad concentration range of the Er^{3+} and Yb^{3+} ions were fabricated using citric route as a function of annealing temperature at 500-1000^{o}C. Effect of broad co-dopants concentration and sintering temperature on structural and up-conversion properties was investigated in detail by X-ray diffraction techniques and optical spectroscopy. TEM technique was used to estimate a mean particle size, that was around 30 nm for the inorganic product annealed at 600^{o}C. Up-conversion emission color tuning was achieved by the particle size control. Power dependence of the green and red emission was found as result of temperature determination in operating range of the $SrTiO_3$ nanoparticles and a candidate for the fast and local microscopic heating and heat release induced by IR irradiation. The color changed from white-red-yellow-green upon increase of sintering temperature inducing changes in surface-to-volume ratio and number of optically active ions in particle surface regions. Cytotoxic activity of nanoparticles on human red blood cells was investigated showing no harmful effects up to particles concentration of 0.1 mg/ml. The cytotoxic response of colloidal suspension of nanoparticles to RBC cells was connected with strong affinity of the $SrTiO_3$ particles to the cell membranes blocking transport of important biological solutes.

Keywords. Nanoparticles, $SrTiO_3$, up-conversion, colour tuning, RBC cells

1. Introduction

Constantly growing interest in perovskite family (ABO_3) forces researchers to focus more efforts on development of new synthetic approaches towards this interesting group of compounds. Strontium titanate ($SrTiO_3$) belongs to the most known representative of the perovskites due to its physicochemical properties being a basis of numerous applications as low voltage electron excitation displays [1], photocatalyst [2], microwave devices [3], gas sensors [4] etc.

In accordance with literature data, $SrTiO_3$ transforms from tetragonal to cubic structure as follows [5]:

$$I4/mcm \xleftrightarrow{105K} Pm\bar{3}m \quad . (1)$$

The differences of the electronic structure and dielectric functions depending on the crystal structure are still a basic of interest for these materials. However, the photoluminescence properties of $SrTiO_3$ doped with trivalent lanthanides are relatively less studied and the most articles have been devoted to the Eu^{3+} or Pr^{3+} ions in this host [1, 6, 7, 8, 9]. Only several papers have dealt with co-doping of nanoparticles with Er^{3+} and Yb^{3+} pairs [10, 11, 12]. Recently, up-converting particles are of great significance in biological applications due to the anti-Stokes emission induced by NIR-excitation covering the optical biological window [13]. High thermal, chemical, physical stability, transparency in VIS region as well as low phonon frequency qualify the $SrTiO_3$ as a potentially effective host matrix for up-conversion [18]. Furthermore, the $SrTiO_3$ is an attractive bioactive material used as one of the main ingredients of injectable acrylic bone cements for vertebroplasty [14] as well as an active layer of the Ti-based osteoporotic bone implants [15]. Therefore, development of the strontium ion(s) releasing implants or cements are of high importance in stimulation of bone formation and inhibition of bone resorption especially in treatment of osteoporosis [15]. Possibility of the bio-imaging of the $SrTiO_3$: Er^{3+}/Yb^{3+} an outer implant layer might be useful in an evaluation of the layer/implant ageing as well as studies of the integration of the implant with bone tissue by observation of the ion diffusion upon possible re-build of the boundary tissue [16]. It has been proved that orally administered Sr^{2+} ions cannot effectively reach the implant - tissue interface thus $SrTiO_3$ deposited on implants will directly release the Sr^{2+} locally promoting bone formation. In the case of the cement materials it is necessary to study the toxic effects of particular ingredients. The high risk of postoperative deep-vein thrombosis (DVT) could be associated with release of cement substances. Thus, the tests of chemical substances present in the cement material on blood compatibility are of great significance [17]. There are several techniques already used for fabrication of the $SrTiO_3$ nanoparticles such as solvothermal [19], hydrothermal processing [20], polymeric precursor method [4], sol-gel [21], combustion [22] etc. The main advantages of these techniques, in contrast to the classical solid state reaction [23], are better control over - structural purity, ease of doping, homogeneity, agglomeration and particles morphology. Moreover, no thorough studies were performed on optimization of dopant concentrations, their influence on up-conversion process efficiency nor grain size effect.

Thus, the main goals of the present work were devoted to thorough study of influence of sintering temperature and dopants concentration on the structural properties of the $SrTiO_3$ matrix, evaluation of the optimal doping levels of the Er^{3+} and Yb^{3+} ion pairs as well as effect of the particle size on the up-conversion process of the $SrTiO_3:Er^{3+}/Yb^{3+}$ nanoparticles. The blood compatibility tests of potential cement material were conducted using human red blood cells (RBC).

2. Experimental

Structure analysis of the $SrTiO_3:Er^{3+}/Yb^{3+}$ nanoparticles was based on measurements of XRD patterns by collecting the data in 2Θ range of 5–120° with X'Pert PRO X-ray diffractometer (Cu, Kα1: 1.54060 Å) (PANalytical). The average particle size was calculated using Scherrer's formula:

$$D = \frac{k\lambda}{\cos\Theta\sqrt{\beta^2 - \beta_0^2}}, \quad (2)$$

the symbols represent D – the mean grain size; β_0 –apparatus broadening; β – full width at half maximum; Θ - reflection angle; k constant (usually equal to 0.9), and λ is an X-ray wavelength [24]. The microstructure and morphology of nanoparticles were studied using high resolution transmission electron microscope (HRTEM) Philips CM-20 Super Twin microscope operating at 200 kV. Samples for measurements were directly taken after purification from reaction mixture with ethanol making particle suspension. Afterwards a droplet of colloid was deposited on a copper microscope grid covered with perforated carbon and gently dried. The mean size of particles was evaluated using volume weighted formula:

$$d_{av} = \frac{\sum n_i d_i^4}{\sum n_i d_i^3}, \quad (3)$$

where d_{av} is the average particle size, n number of particles and d represents particle diameter. Elemental analysis was carried out using a scanning electron microscope FEI Nova NanoSEM 230 equipped with EDX spectrometer (EDAX PegasusXM4). Up to 15 measurements were made from different random areas for each sample in order to achieve satisfactory statistics. Polycrystalline infrared spectra were measured with a Biorad 575C FT-IR spectrometer in KBr suspension for the 1200-400 cm^{-1} region and in Nujol suspension for the 500-50 cm^{-1} region. The up-conversion luminescence spectra were recorded using Jobin Yvon THR 1000 monochromator equipped with a Hamamatsu R928 photomultiplier and a 1200 grooves/mm holographic grating. As an excitation source, continuous 975 nm line of 1.5 W laser diode was used. The luminescence decay times were measured utilizing a LeCroy Wave Surfer

oscilloscope using pulsed 975 nm line of 10 mJ Ti:sapphire laser pumped by the second harmonic of the YAG:Nd^{3+} laser 532 nm line. The power dependence of the up-conversion emission intensity was measured using a miniature fiber spectrometer (Avantes, Netherlands, spectral resolution ~3 nm) and 975 nm laser diode (CNI laser, China). The data was fitted according to the following formula:

$$I_{UPC} = I_{in}^{N}, \quad (4)$$

allowing for estimation of the order of the up-conversion process N showing the photons number required for anti-Stokes emission. All recorded spectra were corrected according to the apparatus response.

Synthesis of $SrTiO_3$:Er^{3+}/Yb^{3+} nanoparticles

$SrTiO_3$ nanoparticles doped with Er^{3+} and Yb^{3+} ions were prepared using relatively fast and economic citric route as a function of either Er^{3+} (0.5 - 2 mol%) and Yb^{3+} (5 - 20 mol%) wide concentrations in order to study the dopant effect. As a matter of fact a high temperature treatment (500 to 1000^{o}C for 3 hrs) was applied to investigate the effect of particle size on structure and luminescence properties. Therefore, preparation procedure of particles is given basing on the $SrTiO_3$ sample with 0.5 mol% of the Er^{3+} and 5 mol% of the Yb^{3+} cations, respectively. The synthesis involved usage of $Sr(NO_3)_2$ (99.999 % Alfa Aesar), $Ti(OC_4H_9)_4$ (99% Alfa Aesar), Yb_2O_3 (99.99 % Alfa Aesar) and Er_2O_3 (99.99 % Alfa Aesar) as a main chemicals as well as citric acid (99.95 % Alfa Aesar) as an organic filler and complexing agent. Stoichiometric amounts of Yb_2O_3 (0.0493 g) and Er_2O_3 (0.0048 g) were suspended in distilled water and subsequently digested in excess of the HNO_3 (ultra-anal Avantor Performance Materials) and recrystallized three times. Afterwards Yb^{3+}, Er^{3+} nitrates were dissolved in water and $Sr(NO_3)_2$ (1 g) was added. Due to the fact, that the $Ti(OC_4H_9)_4$ undergoes fast and uncontrolled hydrolysis upon action of water was stabilized by addition of the 2 ml of 2,4-pentanadione (99 % Alfa Aesar) into 1.7 ml of the $Ti(OC_4H_9)_4$ resulting in creation of yellow and transparent solution. Therefore, the both mixtures were joined and 19.21 g of anhydrous citric acid was added. If necessary appropriate amount of distilled water was added to assure full dissolution of all substances. Further on, glass beaker was carefully heated up at 90^{o}C until black-brown resin was formed. Finally, the by-product was annealed at temperature range of 500 - 1000^{o}C for 3 hrs. Depending on the sintering temperature color of the samples varied from grey-black (below 600^{o}C) and white (above 600^{o}C). Rest of the $SrTiO_3$ Er^{3+}/Yb^{3+} nanoparticles were prepared exactly in the same manner.

Cytotoxic activity of the $SrTiO_3$: 1% Er^{3+} / 5% Yb^{3+} to human red blood cells

Hemolysis assay

Fresh human erythrocyte suspensions were delivered from the blood bank. The erythrocytes were washed three times (3000 rpm, 10 min, +4°C) in the phosphate buffered saline (PBS - 137 mM NaCl, 2.7 mM KCl, 10 mM $NaHPO_4$, 1.76 mM KH_2PO_4, and 10 mM glucose, pH 7.4). After washing, cells were suspended in the buffer at $1.65x10^9$ cells/ml, stored at +4°C and used within 5 h. Red blood cell (RBC) ($1.65x10^8$ cells/ml, ~1.5 hematocrit) then were incubated in the PBS in the presence of test compounds at the concentration 1 mg/ml, 0.1 mg/ml and 0.01 mg/ml for 60 min at 37°C in a shaking water bath. The RBC incubated in the PBS without nanoparticles were taken as the control. Following the incubation, samples were centrifuged (3000 rpm, 10 min, +4°C), and the degree of hemolysis was estimated by monitoring the hemoglobin in the supernatant as previously reported [25]. The results were expressed as a percentage (%) of hemolysis. The hemolysis 0% was taken as the absorbance of the supernatant of the erythrocyte suspensions in the PBS only, while the total hemolysis (100%) was determined when the PBS was replaced by distilled water. Each sample was repeated three times and the experiments were performed 3 times using erythrocytes from different donors.

Erythrocyte sedimentation rate (ESR)

Erythrocytes ($1.65x10^8$ cells/ml) were incubated with nanoparticles (1 mg/ml, 0.1 mg/ml and 0.01 mg/ml) in Eppendorf vials for 60 min, at 37°C under gentle mixing. The RBC incubated in the PBS without nanoparticles, were taken as a control series. The ESR was recorded using a digital camera.

3. Results and Discussion

Structure analysis

The evolution of crystalline phase of the $SrTiO_3$ nanoparticles co-doped with Er^{3+} and Yb^{3+} was conducted on samples containing 0.5 mol% Er^{3+} and 5 mol% Yb^{3+} as a function of annealing temperature by means of the XRD technique (see Figure 1). As it can be seen the sample heat treated at 500°C contains only an amorphous product with significant amount of not fully fired organics (black powder color). This situation is starting to change above 550°C where the formation of semi-phases of Yb_2O_3, TiO_2 (broad peaks around 22.5 and 27.5 2Θ) and traces of the $SrTiO_3$ (2Θ at 32.3° and 46.2°) can be detected. However, after exciding 600°C the reactants are starting to finally form pure phase of the desired perovskite without presence of any impurities or amorphous phase and powders are white-colored. Further, an

increase of annealing temperature up to 1000°C results only in narrowing of diffraction peaks (grain growth) and better product crystallinity (higher reflection signal). The mean grain size was calculated using Scherrer's equation taking into consideration non-split and separate reflections only. The expected size growth was noticed from 20 nm above 39 nm depending on the temperature of thermal treatment as indicated by decrease of FWHM of the peak (full width at half maximum) in Figure 1.

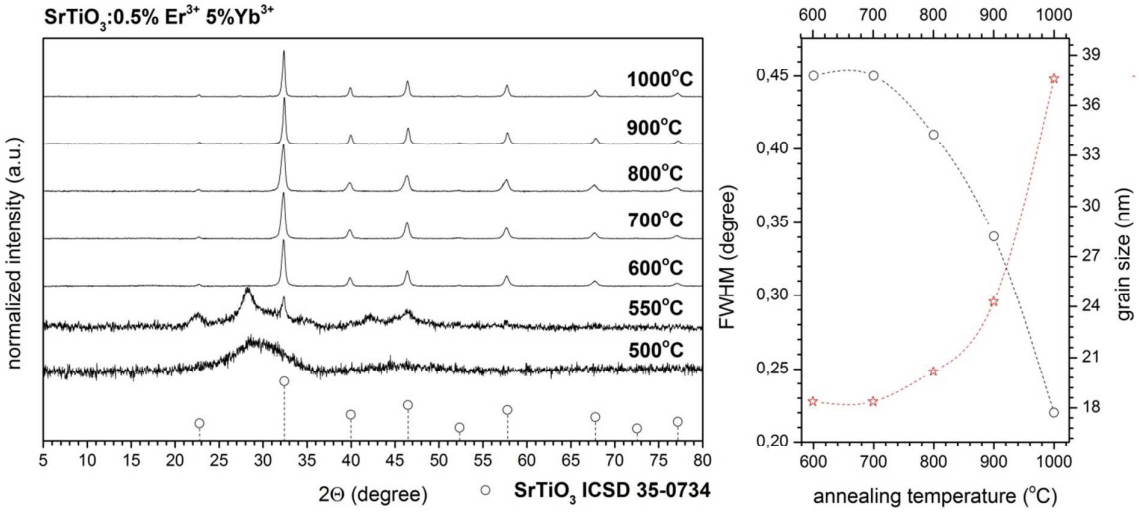

Fig. 1. Temperature evolution of the $SrTiO_3$ 0.5% Er^{3+}/ 5% Yb^{3+} crystal structure (left) as well as FWHM and grain size temperature dependence (right).

The effect of Er^{3+} and Yb^{3+} doping was investigated (see supplementary Figure 1s) for broad concentration ranges as well. The optimization of dopants concentration is extremely important in view of inducing functional property of the $SrTiO_3$ *i.e.* up-conversion. The relation between dopants on up-conversion efficiency will be discussed later. In fact, for the samples with constant Yb^{3+} ions concentration set at 5 mol% there is no influence of increasing Er^{3+} ions amount up to 2 mol% on structural purity. Higher doping levels of the Er^{3+} ions were not studied due to an increase of its content is detrimental for emission properties (vide concentration quenching). Whereas, a specific amount of the Yb^{3+} ions has great implications on luminescence properties because of Yb^{3+} ions play an important role of emission sensitizer. In the case of Yb^{3+} ions, it can be clearly seen that up to 15 mol% the structure of the $SrTiO_3$ remained unchanged. However, further increase of number of the Yb^{3+} ions above 20 mol% inhibits the crystallization of final phase. The XRD pattern appears the same as for the sample heat treated at 550°C. Indeed, an increase of temperature above 700°C leads to the formation of the $SrTiO_3$ (see supplementary Figure 2s.) but with presence of small amount of impurity phases. Moreover, the further increase of the temperature results in phase

separation and formation of multiphase product (supplementary Figure 3s). Therefore, the solubility limit of the Yb^{3+} ions in the $SrTiO_3$ is 15 mol%. It is also important to emphasize that for highly concentrated samples phase separation is also induced by temperature factor affecting the thermodynamic equilibrium (see supplementary Figure 4s.) As it can be seen multiphase products are obtained for samples with the Yb^{3+} ions concentration higher than 10 mol% starting from 900°C. In the context of material purity it seems that the $SrTiO_3$ doped with 0.5 mol% of the Er^{3+} and 5 mol% Yb^{3+} ions together with 1 mol% are optimal. The sample with 2 mol% of Er^{3+} and with Yb^{3+} ions content above 10 mol% of Yb^{3+} are already multiphase at 900°C (supplementary Figure 5s).

In order to shed more light on structural properties of the $SrTiO_3$ doped with Er^{3+} and Yb^{3+} ions Rietveld refinement [26] using isotropic approach [27],[28] in Maud 2.5 software was performed. The result of fitting on representative sample of the 0.5% Er^{3+},5% Yb^{3+}:$SrTiO_3$ heated at 600°C is presented in Figure 2, whereas calculated values of cell parameters were gathered in table I and II.

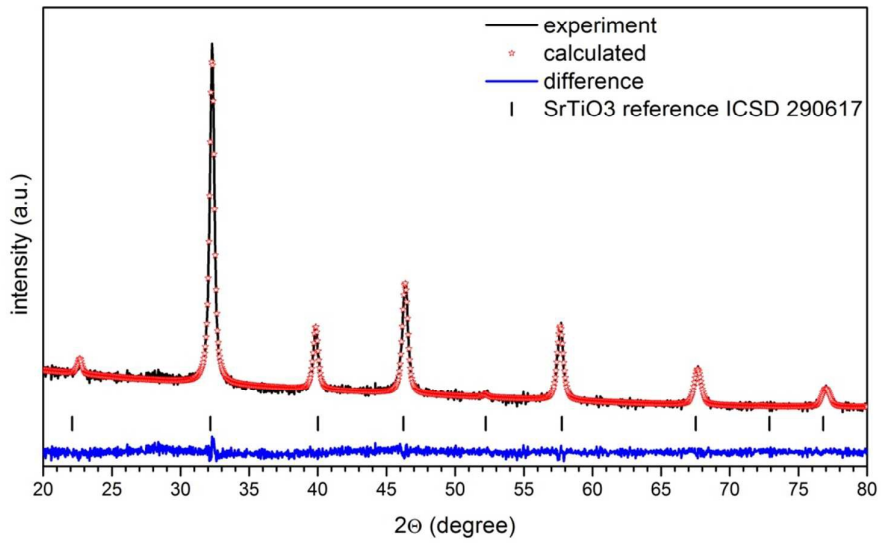

Fig. 2. XRD pattern (back line) and result of the Rietveld analysis of the $SrTiO_3$ 0.5% Er^{3+}/ 5% Yb^{3+} nanoparticles annealed at 600°C.

It is well known that the $SrTiO_3$ crystallizes in cubic structure with the space group $Pm\bar{3}m$ (No. 221), where Sr^{2+} is in twelve fold coordination (1.44 Å) and Ti^{4+} is surrounded by six oxygen anions (0.605 Å). The problem of exact site substitution with rare earth cations (RE^{3+}) in $MTiO_4$ (M - Ca^{2+}, Sr^{2+} and Ba^{2+}) perovskites is still not fully comprehend. Basing only on

comparison of ionic radii substitution of the Er^{3+} and Yb^{3+} ions would occur most likely at Sr^{2+} site due to the best compatibility of the ionic radii even though there is not data regarding the radii of twelve fold coordination of both dopants (Er^{3+} at C.N. 9 - 1.062 Å , at C.N. 6 -0.89 Å , Yb^{3+} at C.N. 9 - 1.042 Å, at C.N. 6 - 0.868 Å). However, the issue is not clearly resolved since Tsur et al. [30] showed that in the case of $BaTiO_3$ so called tolerance factor *t*:

$$t = \frac{r_A + r_O}{\sqrt{2}(r_B + r_O)}, (5)$$

has to be taken into account where r_A, r_B and r_O are ionic radii of the *A*, *B* and *O* ions with specific coordinations numbers. For the ideal perovskite tolerance factor reaches value of 1 which is the case of $SrTiO_3$.

Table I. Results of the Rietveld refinement of the $SrTiO_3$ Er^{3+}/Yb^{3+} nanoparticles as a function of sintering temperature and dopants concentration.

Temperature	a (Å)	V (Å^3)	grain size (nm)	R_w (%)
0.5% Er 5% Yb 600°C	3.9152(1)	60.01(6)	36.98±0.01	3.33
0.5% Er 5% Yb 700°C	3.9162(0)	60.06(1)	33.92±0.01	3.41
0.5% Er 5% Yb 800°C	3.9208(5)	60.27(5)	34.95±0.01	3.75
0.5% Er 5% Yb 900°C	3.9123(3)	59.88(3)	52.71±0.01	3.73
0.5% Er 5% Yb 1000°C	3.9141(9)	59.96(9)	59.62±0.01	4.28
Er^{3+} concentration	**a (Å)**	**V (Å^3)**	**grain size (nm)**	**R_w (%)**
0.5% Er 5% Yb 600°C	3.9152(1)	60.01(6)	36.98±0.01	3.33
1% Er 5% Yb 600°C	3.9160(8)	60.05(6)	36.08±0.01	3.09
2% Er 5% Yb 600°C	3.9153(1)	60.02(0)	32.99±0.01	2.89
Yb^{3+} concentration	**a (Å)**	**V (Å^3)**	**grain size (nm)**	**R_w (%)**
0.5% Er 5% Yb 600°C	3.9152(1)	60.01(6)	36.98±0.01	3.33
0.5% Er 10% Yb 600°C	3.9158(8)	60.04(7)	35.47±0.01	2.71
0.5% Er 15% Yb 600°C	3.9141(2)	59.96(6)	30.89±0.01	3.21
0.5% Er 20% Yb 600°C	3.9131(7)	59.92(2)	21.92±0.01	3.46

Therefore, it is expected that if the incorporation at *A* site results into tolerance factor closer to 1 than incorporation into the other site is not preferred. Thus ions with smaller radii than 0.87 Å will occupy the *B*-site whereas larger ones with r(RE_{VI}^{3+}) > 0.94 Å the *A* site [30]. Since the ionic radii for twelve fold coordination of Er^{3+} and Yb^{3+} are unknown calculations were done only taking into consideration of six-fold coordinations.

Table II. Atomic parameters of the $SrTiO_3$ 0.5% Er^{3+}/5% Yb^{3+} annealed at 600°C.

Sample	SrTiO3 0.5% Er^{3+}/5% Yb^{3+}, Z = 1					
Space group	Cubic ***Pm-3m*** (No. 221)					
Calculated cell parameters	a = 3.9152(1) Å V = 60.01(6) Å^3					
R_w	3.33%					
R_{wnb}	3.25%					
R_{all}	2.42%					
R_{nb}	3.21%					
σ	2.18%					
Selected contacts						
Er|Sr|Yb – Yb|Sr|Er	3.9152 Å					
Er|Sr|Yb – O	2.7685 Å					
Ti – Ti	3.9152 Å					
Ti – O	1.9576 Å					
Er|Sr|Yb – Ti	3.3907 Å					
Er|Sr|Yb – O – Ti	90.00 °					
Atom	**Wyckoff positions**	**x**	**y**	**z**	B_{iso}	**Occ. (<1)**
Sr1	*1a*	0	0	0	0.3017(8)	0.945
Til1	*1b*	0.5	0.5	0.5	0.1020(1)	
O1	*3c*	0.5	0.5	0.5	0.2024(2)	
Yb1	*1a*	0	0	0	0.3010(4))	0.05
Er1	*1a*	0	0	0	0.3010(5)	0.005

Results are showing, that the Yb^{3+} (t is 0.885) substitution should occur mainly at B-site whereas the Er^{3+} (t equal to 0.876) is at intermediate position meaning that both sites could be replaced. This is in accordance with previous reports on dual character of the Er^{3+} [30]. Thus, it is actually quite difficult to differentiate the positions of the RE^{3+} and more data is needed to provide more convincing evidence. Definitely, the problem of exact substitution position is directly related to the dopant solubility and thermodynamic behavior of given compound. The site preference is even more complex for highly doped materials. As it can be seen cell parameters of the Er^{3+} and Yb^{3+} ions doped $SrTiO_3$ did not show strong differences upon sintering temperature up to 800°C as well as Er^{3+} ions doping where the cell volume changes only a little (expected shrinkage). Almost the same trend stands for Yb^{3+} ions concentration showing no effect up to 10 mol%. Above that value, the phase separation occurs leading in formation of secondary compounds. In the other words, the effective concentration of the Yb^{3+} ions was lower than 15 or 20 mol% in the $SrTiO_3$ structure. Another factor influencing the structural properties *i.e.* grain size has to be taken into account as well. It is well known

that reduction of the particle size could contribute to the creation of negative pressure on the crystal lattice eventually leading a lattice cell volume expansion [31], [32]. Therefore, two adverse effects are most likely present in the same time - effect of doping which leads to shrinking of the cell volume as well as size effect resulting in cell expansion for the smallest particles annealed below 800^{o}C. General conclusion might be drawn that the Er^{3+} and Yb^{3+} dopants are increasing the crystallization temperature and decreasing the growth of $SrTiO_3$particles as well as lead to the phase separation at critical concentration limits and sintering temperature.

For the $Pm\bar{3}m$ structure of the $SrTiO_3$ group theory predicts only three IR-active modes of F_{2u} symmetry [33,34]. The IR reflection spectra show that the transverse optical (TO) modes of the $SrTiO_3$ should be observed at 89, 175 and 544 cm^{-1}. The corresponding longitudinal optical (LO) modes are expected at 172, 475 and 796 cm^{-1}. The lowest (highest) frequency mode corresponds to Ti-O-Ti bending (Ti-O stretching) vibrations. The band at 175 cm^{-1} (TO) and 475 cm^{-1} (LO) involves bending vibrations of Ti-O bonds and translations of Sr^{2+} cations[33]. For a polycrystalline and nanocrystalline sample, shape and maximum intensity of an IR band can be very dependent upon the size and shape of crystallites due to the long-range Coulomb forces. In particular, the maximum intensity may shift towards LO frequency and a band may become very asymmetric[35,36]. The IR spectra of the Er^{3+}/Yb^{3+}:$SrTiO_3$ showed presence of a strong band in the mid-IR region at about 560 cm^{-1} (supplementary Figure 6s). This band could be attributed to the Ti-O stretching mode and its maximum intensity is close to the expected TO value at 544 cm^{-1} [33] One can note presence of a broad and weaker band near about 735 cm^{-1}. Frequency of this band is close to the expected LO value at 796 cm^{-1}. Similar band was also observed for pure nanocrystalline $SrTiO_3$ [37]. Far-IR spectra show presence of two bands near 160 and 200-250 cm^{-1} (supplementary Figure7s). The higher frequency band was very broad and asymmetric, and this feature may again be attributed to very large LO-TO splitting of the corresponding mode. The lower frequency band was relatively narrow and its maximum is about 15 cm^{-1} below the LO value. The shape of the mid-IR contour changed significantly with increasing concentration of the Yb^{3+} ions. In particular, the bands become broader and intensity of the higher frequency band significantly increases. This behavior indicates that TiO_6 octahedra were affected by Yb^{3+} ions doping. This conclusion was further supported by the far-IR data, which showed significant changes with increasing concentration of the Yb^{3+} ions also for the lowest frequency Ti-O-Ti bending mode at 160 cm^{-1}. Interestingly, this mode shifts towards higher frequency with increasing concentration of the Yb^{3+} (from 155 cm^{-1} for 5% of Yb^{3+} to 165 cm^{-1} for 20 % of Yb^{3+}) whereas the former study of neodymium-doped $SrTiO_3$ showed an opposite behavior [34].

Furthermore, intensity of this band significantly decreased. It is also worth noting that IR data for pure and neodymium-doped $SrTiO_3$ showed weak influence of doping on shape of the mid-IR band corresponding to the Ti-O stretching mode but strong intensity decrease of the broad band at 200-250 cm^{-1} corresponding to the coupled Ti-O-Ti bending and Sr^{2+} translational modes. In contrast to the Nd^{3+}:$SrTiO_3$: sample containing both lanthanides Er^{3+} and Yb^{3+} did not show any intensity decrease of the broad far-IR band with increasing concentration of the Yb^{3+}ions. In conclusion, IR data for the Er^{3+}/Yb^{3+}:$SrTiO_3$ show opposite behavior than the IR spectra reported for the Nd^{3+}:$SrTiO_3$. In the later case, changes in the IR spectra are consistent with the postulated preferential occupation of the Sr^{2+} sites. However, data indicate that in the Er^{3+}/Yb^{3+}:$SrTiO_3$ samples, the ytterbium ions occupy predominantly the titanium sites, as evidenced by significant changes upon doping of the IR bands corresponding to the Ti-O stretching and bending vibrations. No striking effect of the Er^{3+} ions were found on vibrations of the Sr^{2+} ions most likely due to the low concentration of the Er^{3+} ions.

TEM (Transmission Electron Microscopy) analysis was performed (see Figure 3) in order to estimate the mean particle grain size, size distribution as well as influence of annealing temperature on particle growth. As it can be seen the particle size is strongly dependent on sintering temperature and for 600^{o}C mostly 20-30 nm irregular and forming aggregates particles are detected. Upon heating fast particle growth was found and grain size for the 800^{o}C treated $SrTiO_3$ is around 50-60 nm whereas above 1000^{o}C particles are much bigger (above 100 nm). Comparison of the TEM size estimation with the Rietveld fits gives quite good correspondence especially for the lower thermally treated samples. An application of higher temperature leads to difficult to control particle growth, ongoing agglomeration pointing out on the typical Ostwald ripening growth mechanism. Additionally, SAED (Selected Area Electron Diffraction) patterns revealed presence of well developed spotty rings at positions and distances corresponding with the reference standard of the $SrTiO_3$.

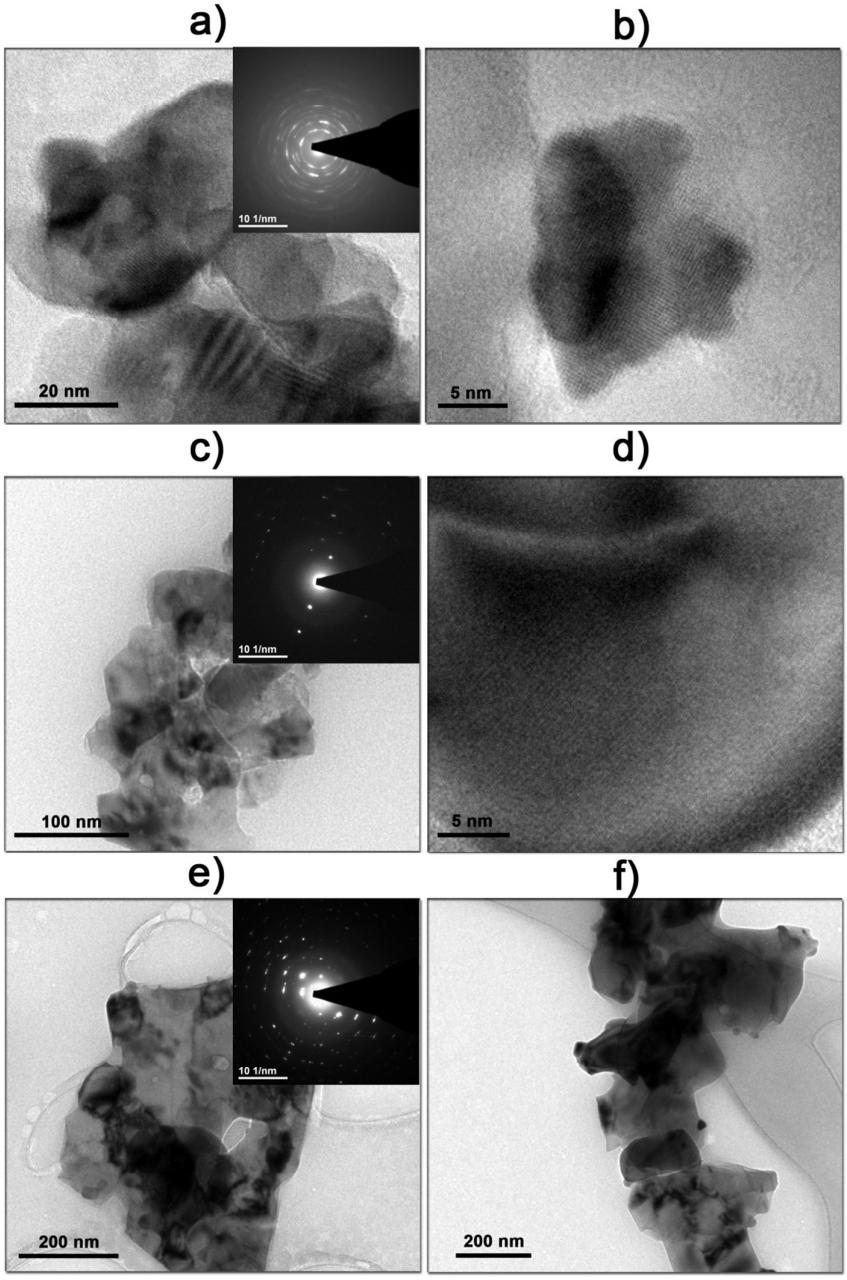

Figure 3. TEM images of the $SrTiO_3$: 0.5% Er^{3+} / 5% Yb^{3+} nanoparticles sintered at 600°C (a, b), 800°C (c, d) and 1000°C (e, f). Insets show SAED images.

The concentrations of the Er^{3+} and Yb^{3+} ions (nominal 1 mol% and 5-20 mol%) in the $SrTiO_3$ nanoparticles was evaluated utilizing EDS (Energy-Dispersive Spectroscopy) analysis (supplementary Figure 8s). As it can be seen the contents of respective lanthanides are close to the desired one with rather small deviations. The deviation from the nominal content results in a variation of distribution of the Er^{3+} and Yb^{3+} ions in the crystal matrix *i.e.* presence of dopants in the close-to-surface area since surface to volume ratio is higher in nanoparticles than in a bulk material. On the other hand, surface layer enrichment is one of the natural

results of size incompatibility leading to the ion clustering and phase separation upon exceeding critical concentration or sintering temperature [38].

Optical properties

The mechanisms of the up-conversion process, APTE effect (addition de photon par transfer d'energie) existing in the literature also as ETU (energy transfer up-conversion), excited state absorption (ESA) and photon avalanche (PA) were described in a great detail by Auzel [39]. In majority of cases ETU and ESA are most effective. However, it is difficult to distinguish between them especially in the system containing Er^{3+} and Yb^{3+} co-dopants since in order to achieve up-conversion emission both processes involve participation of two photons [39]. The up-conversion emission can be observed in the systems composed of the ions of the same type *i.e.* the Er^{3+} ion but due to the small absorption cross section of the Er^{3+} ion additional doping with so-called sensitizer ion, with large absorption cross section, is necessary in order to significantly improve efficiency. In fact, efficient energy transfer from the emission sensitizer to the activator must take place meaning that there is a need of existence of specific energy levels of both ions in resonance.

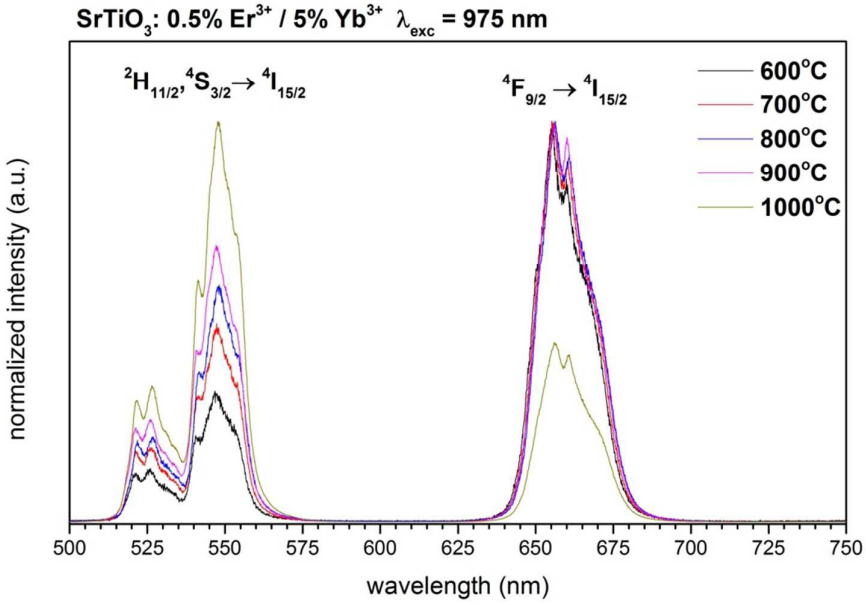

Fig. 5. Up-conversion emission spectra of the $SrTiO_3$ 0.5% Er^{3+} / 5% Yb^{3+} as a function of sintering temperature (particle size).

All of these conditions are fulfilled upon co-doping of the Er^{3+} with Yb^{3+} ions having resonance between electronic transitions of the $^2F_{5/2} \rightarrow {}^2F_{7/2}$ (Yb^{3+}) and the $^4I_{15/2} \rightarrow {}^4I_{11/2}$ (Er^{3+}). Large absorption cross section of Yb^{3+} assures effective absorption of the excitation energy. The representative up-conversion emission spectra of the $SrTiO_3$ co-doped with 0.5%

of Er^{3+} and 5% of Yb^{3+} measured at 300 K and recorded after excitation with 975 nm diode laser as a function of sintering temperature are shown in Figure 5. The spectra consists of typical anti-Stokes emission transitions situated in the green spectral range of 500 - 575 nm ascribed to the $^2H_{11/2} \rightarrow {}^4I_{15/2}$ with maxima at 526.9 nm (18 979 cm^{-1}) and to the $^4S_{3/2} \rightarrow {}^4I_{15/2}$ electronic transitions at 547.8 nm (18 255 cm^{-1}) as well as red region of 625 - 690 nm with the characteristic $^4F_{9/2} \rightarrow {}^4I_{15/2}$ electron transition at 655.9 nm (15 246 cm^{-1}), respectively. As it can be seen the emission spectra were non-homogenously broadened and peaks non- resolved into separate Stark components of each transitions. The most striking observation was seen in constant of an intensity increase of the green bands and a decrease of red transition with the sintering temperature increase or in other words, with particle growth from nanometric size up to submicron scale above 900°C. The most likely the broadening of the anti-Stokes emission peaks would be attributed to the occupation of different crystallographic sites by Er^{3+}, as already suggested by structural data, resulting in the spectral overlap of the Stark components of electron transitions. Additionally, the source of such behavior might be also seen in the presence of structural defects induced by charge compensation effect as well as heterogeneous distribution of the dopants due to the presence of Er^{3+} and/or Yb^{3+} ions on the particles surface enriched regions with lowered symmetry of closest RE^{3+} surroundings.

In order to comprehend the interplay of the green and red up-conversion emission as a function of the Er^{3+} and Yb^{3+} ions concentration, particle size (thermal treatment), and estimate the efficiency of the up-conversion process *GRR* ratio (green-to-red ratio) was calculated [40] in the following manner:

$$GRR = \frac{I(^2H_{11/2}, {}^4S_{3/2} \rightarrow {}^4I_{15/2})}{I(^4F_{9/2} \rightarrow {}^4I_{15/2})}, \quad (6)$$

where numerator is an integral intensity of green bands and denominator defines integral intensity of red transition. Beforehand, it has to be mention that the general rule regarding *GRR* interpretation could be proposed. The higher is the *GRR*, the better performance of up-conversion system could be. It means that the green bands integral intensity increases at the expense of red band than efficiency of the up-conversion increases due to the decrease of contribution of the non-radiative processes such as cross-relaxation and/or multiphonon relaxation processes. Therefore, it is expected that the *GRR* ratio could be strongly dependent not only on the point site symmetry (exact level splitting in crystal field) but also on particle size, dopant concentration or excitation power influencing population of the electronic states [41]. Figures 6 and 7 present the up-conversion emission spectra as well as the *GRR* ratio of the

$SrTiO_3$ particles doped with different Er^{3+} and Yb^{3+} ions concentrations. Among all tested contents of the Er^{3+} ions (0.5 - 2 mol%) the least concentration seems to be the best one since the highest *GRR* ratio was achieved.

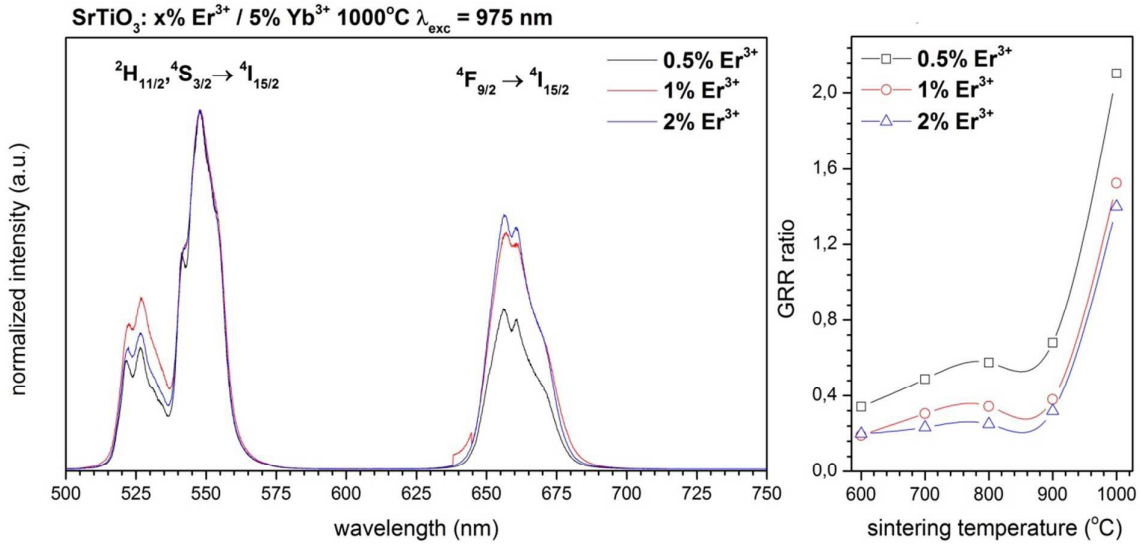

Fig. 6. Up-conversion emission spectra of the $SrTiO_3$ x% Er^{3+} / 5% Yb^{3+} (left) and GRR ratio as a function of sintering temperature and Er^{3+} concentration (right).

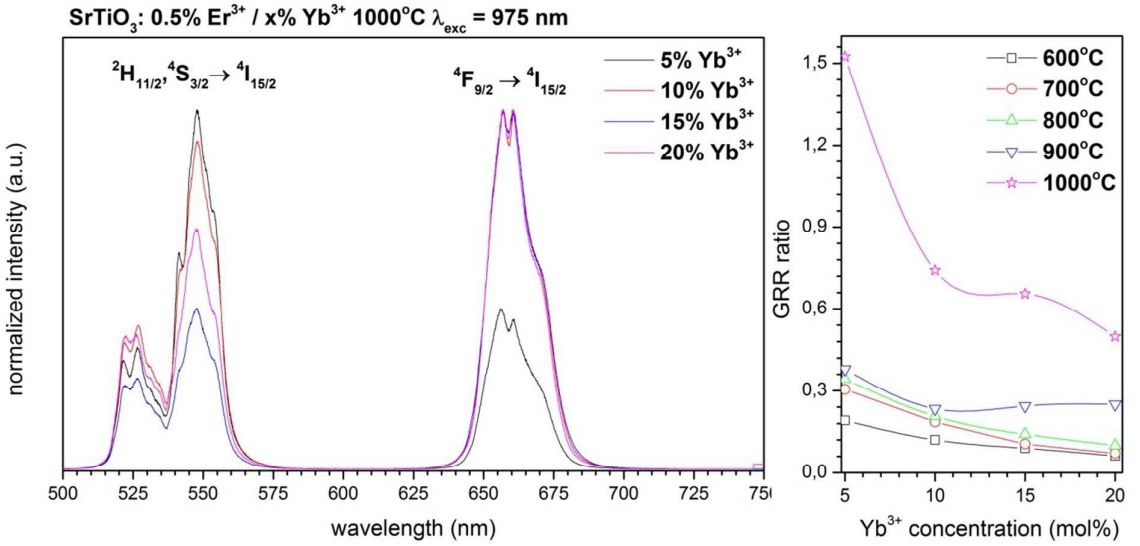

Fig. 7. Up-conversion emission spectra of the $SrTiO_3$ 0.5% Er^{3+} / x% Yb^{3+} (left) and GRR ratio as a function of sintering temperature and Yb^{3+} concentration (right).

In fact, it is well known that contribution of the cross-relaxation processes is strongly dependent on optically active ion concentration. Thus, decreases of the Er^{3+} ions concentration results in minimization of the inter-ionic-interactions which have parasitic effect on the green emission. In the case of the Yb^{3+} sensitizer, increase of its content should be beneficial for the up-conversion since ions are able to harvest more of the IR excitation and directly transfer extra photons to the Er^{3+} ions[42]. However, as it can be seen in Figure 7 the

highest *GRR* ratio is obtained for the samples not exceeding 5 mol% of Yb^{3+} ions. Further increase of the Yb^{3+} ions has detrimental effect on up-conversion in this system. Again structural properties have to be taken into account to understand what is actually happening. As it was written earlier, the concentration of Yb^{3+} ions higher than 5 mol% lead to the phase separation of the system and formation of multiphase product. In addition energy transfer in such complex system is influenced by the structural restrictions of new compounds (different symmetry, energy of net phonons etc.). It cannot be excluded that a rising of Yb^{3+} ions concentration might lead also to a back-transfer since one can see that the intensity of the green band decreases with the increasing of Yb^{3+} content as well. Furthermore, the back-transferred energy could benefit in enhanced emission of Yb^{3+} ions. In general, the role of the annealing temperature is directly connected with the particle size. It results in enhancement of the up-conversion efficiency since the *GRR* ratio greatly increased with the particle size.

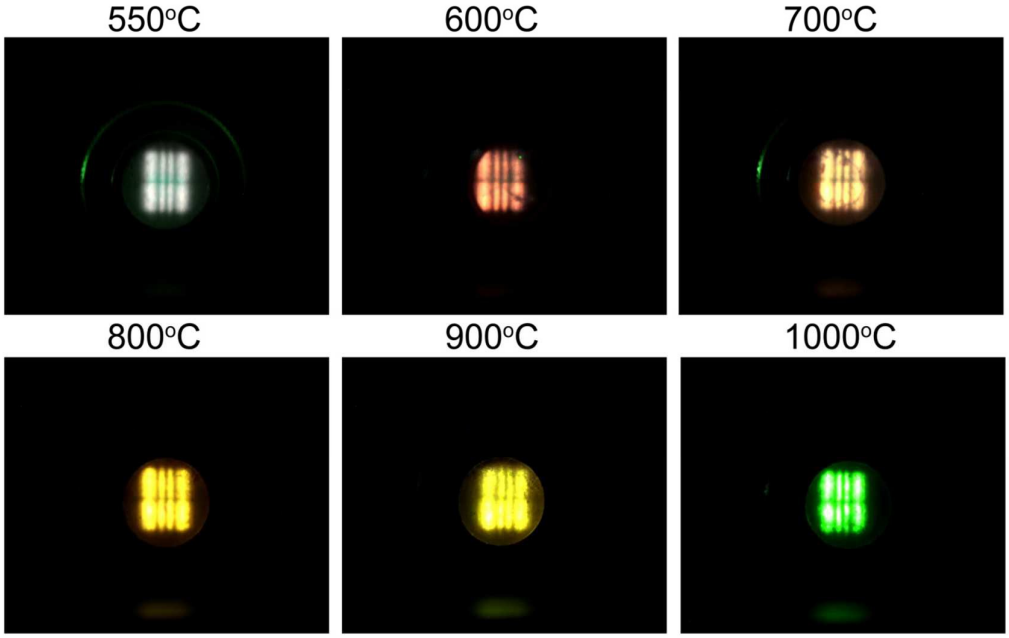

Fig. 8. Up-conversion emission color tuning of the $SrTiO_3$ 0.5% Er^{3+} / 5% Yb^{3+} by growth of particle size induced by thermal treatment.

The highest *GRR* values were obtained for the largest particles. In the case of nanoparticles higher fraction of optically active cations were located closer to the nanoparticles surface. Hence, it was extremely sensitive for non-radiative deactivation caused by impurities, surface states, defects, ion clusters etc. In the context of biological applications, it is important to get as efficient up-conversion as possible with predominant character of the green emission. Nevertheless, the red emitting up-conversion materials might be seen as the drawback. However, it can be the basis in the color tuning by the particle size tailoring. The same feature

is observed in quantum dots (QDs) taking out the advantageous role of quantum confinement effect shaping the energy band gap with particle size[43]. However, in the case of the $SrTiO_3$ color tuning would be based only on playing with the number of optically active ions in close-to-surface regions. As it is shown in Figure 8 the color of the 0.5% Er^{3+}/5% Yb^{3+}:$SrTiO_3$ changed from white through red-yellow-green only through change of the particle size induced by sintering temperature. It has to be underlined that the white emission of 550°C sample is connected with the high concentration of defects and other states, in accordance with the XRD measurement showing only partially crystallization of this powder. Therefore, the color of up-conversion depends on the contribution of non-radiative processes like cross-relaxation and multiphonon relaxation favoring population of the green ($^2H_{11/2}$ and $^4S_{3/2}$) and red ($^4F_{9/2}$) bands depending on the size of particle and/or surface to volume ratio.

It was worth to note that the relative intensity of the both green transitions of the $^2H_{11/2} \rightarrow {}^4I_{15/2}$ and the $^4S_{3/2} \rightarrow {}^4I_{15/2}$ depends on the laser power causing self-heating of the sample. This dependence has practical implication in the field of temperature sensing or in biological applications allowing fast microscopic heating and heat release without incidental damage of health tissues. In fact, since the both levels are close to each other (ΔE = 724 cm^{-1}) their population given as an integrated fluorescence intensity ratio (*FIR*) is driven by Boltzmann's distribution:

$$FIR = \frac{I(^2H_{11/2} \rightarrow {}^4I_{15/2})}{I(^4S_{3/2} \rightarrow {}^4I_{15/2})} = \frac{g_H A_H h\nu_H}{g_S A_S h\nu_S} \exp(-\frac{\Delta E}{kT}) = B\exp(-\frac{\Delta E}{kT}), \quad (7)$$

where g_H and g_s are the degeneracy of the $^2H_{11/2}$ and $^4S_{3/2}$ levels, A_H, A_S and ν_H, ν_S are the spontaneous emission rates and frequencies of the $^2H_{11/2} \rightarrow {}^4I_{15/2}$ and the $^4S_{3/2} \rightarrow {}^4I_{15/2}$ transitions, h is the Planck's constant, k is the Boltzmann's constant (0.6952 $K^{-1}cm^{-1}$), T is absolute temperature and ΔE is the energy gap [44]. Transformation of the equation (7) into linear dependence:

$$\ln(FIR) = \ln(B) + (-\frac{\Delta E}{kT}) = \ln(B) + (-\frac{C}{T}), \quad (8)$$

allows for extraction of B and C constants. Since, the ΔE equals 724 cm^{-1} then calculated C constant is about 1041 K. Further assumption has to be made that sample temperature was 300 K at zero limit of laser power then FIR for room temperature can be estimated by extrapolation of power dependence of FIR giving the value of 0.52 (supplementary Fig. 9s). Hence, taking into account equation (8) $ln(B)$ was 1.76 being consistent with previously reported range for this constant $1.5 \leq ln(B) \leq 2.5$ [45]. Thus for the highest optical laser power of

1.59 W (50.61 W/cm^2) and *FIR* = 1.43 *T* is 743 K determining the operating range of the studied system for the laser power.

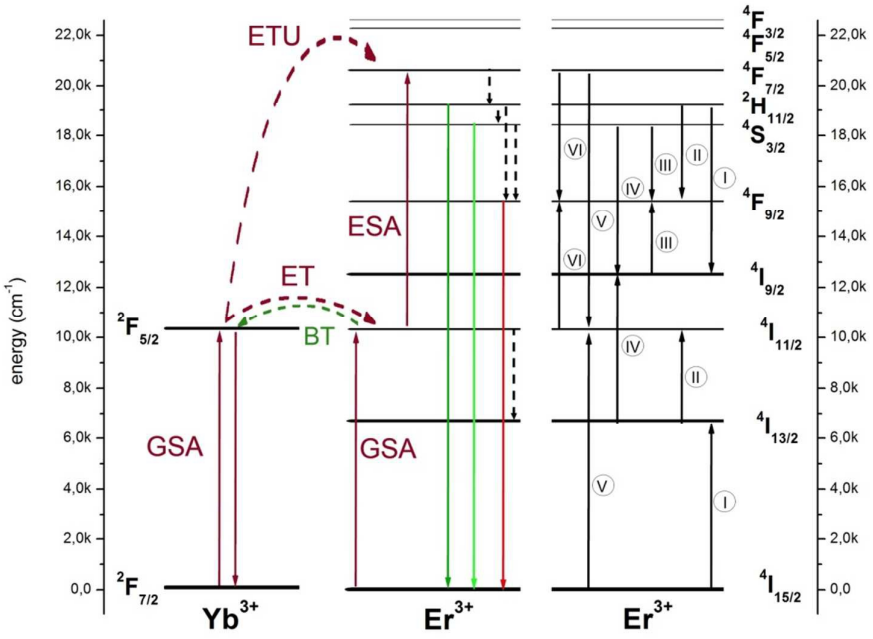

Fig. 9. Simplified energy level scheme presenting up-conversion, CR (numbered circles) and MPR (dot black lines) processes (description in the text).

Simplified energy level diagram was proposed describing the most important processes contributing and accompanying to the up-conversion of the Er^{3+} and Yb^{3+} ions co-doped $SrTiO_3$ nanoparticles (Figure 9). Instantaneously, the electrons of Yb^{3+} and Er^{3+} ions were excited by NIR photons from the ground states $^2F_{7/2}$ and $^4I_{15/2}$ to the $^2F_{5/2}$ and $^4I_{11/2}$ levels by ground state absorption process (GSA). Next photon moved electrons directly from the $^4I_{11/2}$ level to the $^4F_{7/2}$ by the excited state absorption (ESA) in Er^{3+} ions. However, due to the large absorption cross section of Yb^{3+} ions majority of the excitation energy was absorbed by Yb^{3+} ions. Therefore, electrons from the $^2F_{5/2}$ level were transferred to the $^4I_{11/2}$ level of the Er^{3+} ions by energy transfer (ET) and/or to the $^4F_{7/2}$ level of the Er^{3+} ions by energy transfer up-conversion process(ETU). In fact, the ET and ETU demand participation of two photons to be realized. Subsequently, electrons from the $^4F_{7/2}$ level relaxed non-radiatively to the $^2H_{11/2}$ and $^4S_{3/2}$ levels via multiphonon relaxation process (MPR). Afterwards, radiative de-excitation could occurred to the ground $^4I_{15/2}$ level resulting in green emissions. Since, the energy difference between $^2H_{11/2}$ and $^4S_{3/2}$ is small MPR would be effective in feeding of the lower level. The competition of radiative and non-radiative processes part of the electrons was depopulated to the $^4F_{9/2}$ level due to the MPR between the $^2H_{11/2}$ + $^4S_{3/2}$ levels and/or cross

relaxation (CR) process. The interplay between the green emission and red one could be tuned by careful selection of host lattice (less energetic phonons), balance of co-dopants concentration (limitation of CRs), particle size (surface-to-volume ratio) and synthetic parameters. It is well known that the CR is concentration and laser-power sensitive. As it can be seen that the several CRs were probable:

$$(^2H_{11/2} + {}^4S_{3/2}, {}^4I_{15/2}) \rightarrow (^4I_{9/2}, {}^4I_{13/2}), \text{(I)}$$

$$(^2H_{11/2} + {}^4S_{3/2}, {}^4I_{13/2}) \rightarrow (^4F_{9/2}, {}^4I_{11/2}), \text{(II)}$$

$$(^4S_{3/2}, {}^4I_{9/2}) \rightarrow (^4F_{9/2}, {}^4F_{9/2}), \text{(III)}$$

$$(^4S_{3/2}, {}^4I_{13/2}) \rightarrow (^4I_{9/2}, {}^4I_{9/2}), \text{(IV)}$$

$$(^4I_{11/2}, {}^4I_{11/2}) \rightarrow (^4I_{15/2}, {}^4F_{7/2}), \text{(V)}$$

$$(^4I_{11/2}, {}^4F_{7/2}) \rightarrow (^4F_{9/2}, {}^4F_{9/2}), \text{(VI)}$$

leading to the strong depopulation of green bands, decrease of the *GRR* ratio and enhanced red and NIR emissions of Er^{3+} ions. These processes would be even more effective upon increase of Er^{3+} ions concentration in the host lattice. In the case of Yb^{3+} ions concentration increase most probably have had detrimental effect on up-conversion efficiency due to the possibility of energy back transfer from the $^4I_{11/2}$ level of Er^{3+} ions to the $^2F_{5/2}$ level. Finally, the emission of Yb^{3+} ions from upper levels to the $^2F_{7/2}$ ground state showed that no green emission was enhanced by Yb^{3+} ions doping above 5 mol%.

The power dependence of both green transitions ($^2H_{11/2} \rightarrow {}^4I_{15/2}$ and $^4S_{3/2} \rightarrow {}^4I_{15/2}$) and red ($^4F_{9/2} \rightarrow {}^4I_{15/2}$) emissions were studied (Figure 10) as a function of the sintering temperature. The linear fit of experimental data lead to the values of around 1 for the $^4S_{3/2} \rightarrow {}^4I_{15/2}$ which was almost independent on the heating temperature. In the case of the $^2H_{11/2} \rightarrow {}^4I_{15/2}$ level the *n* value gradually increased from 1.3 up to almost 1.6 for the largest particles. The value of pump power dependence of the red band remains almost unchanged and was around 1. As stated by Pollnau, in the classical case, both slopes of the green and red emission tend to be close to 2. However, if the $^4F_{9/2}$ level is populated from $^4I_{15/2}$ level through ETU slope of power dependence, the red band should be close to 3 (three photon process) [46]. Actually, none of these stands for the Er^{3+}/Yb^{3+} co-doped $SrTiO_3$ samples, only for the 1000°C treated sample the slope of green emission had value close to 2. Thus, following Liu [47] low values of *n* being close to 1 could be indication of increased role of strong non-radiative processes which is consistent with the *GRR* behavior.

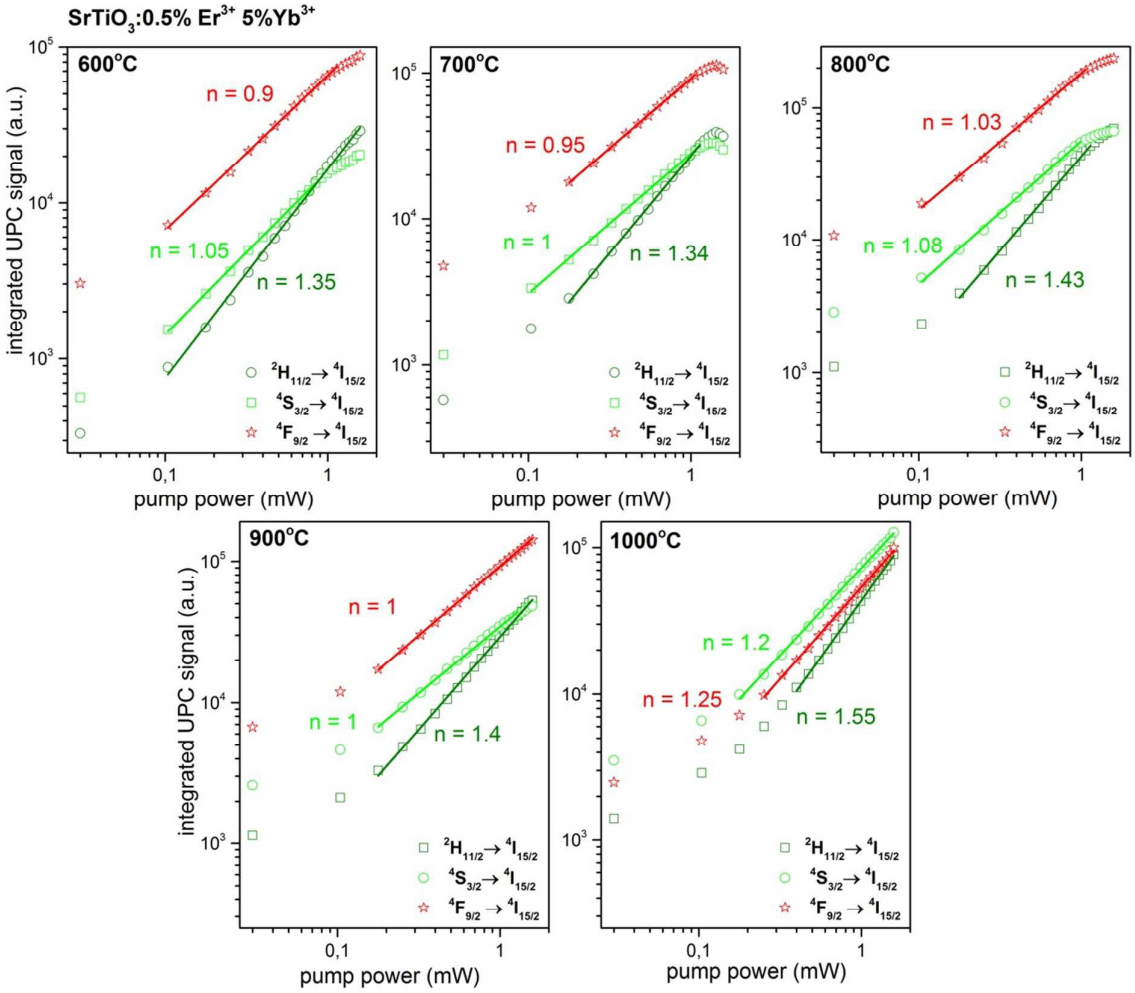

Figure 10. Power dependence of the SrTiO3 doped with 0.5 mol% Er^{3+} and 5 mol% Yb^{3+} ions as a function of annealing temperature.

It is also interesting to note that below 900°C, samples with the particles size below 100 nm (TEM analysis) saturation of population of both green and red energy levels were achieved.

The luminescence decay times of the $SrTiO_3$ co-doped with different concentration of Er^{3+} and optimal 5 mol% Yb^{3+} ions content were recorded for the green and red transitions as a function of sintering temperature (see Figure 11 and 12). The decay curves were clearly non-exponential. Thus, values of lifetimes were calculated as the effective emission decay time using following expression:

$$\tau_m = \frac{\int_0^{\infty} tI(t)dt}{\int_0^{\infty} I(t)dt} \cong \frac{\int_0^{t^{max}} tI(t)dt}{\int_0^{t^{max}} I(t)dt}, \quad (9)$$

where *I(t)* represents the luminescence intensity at time *t* corrected for the background and the integrals are evaluated on a range $0 < t < t^{max}$ where $t^{max} >> \tau_m$ [48].

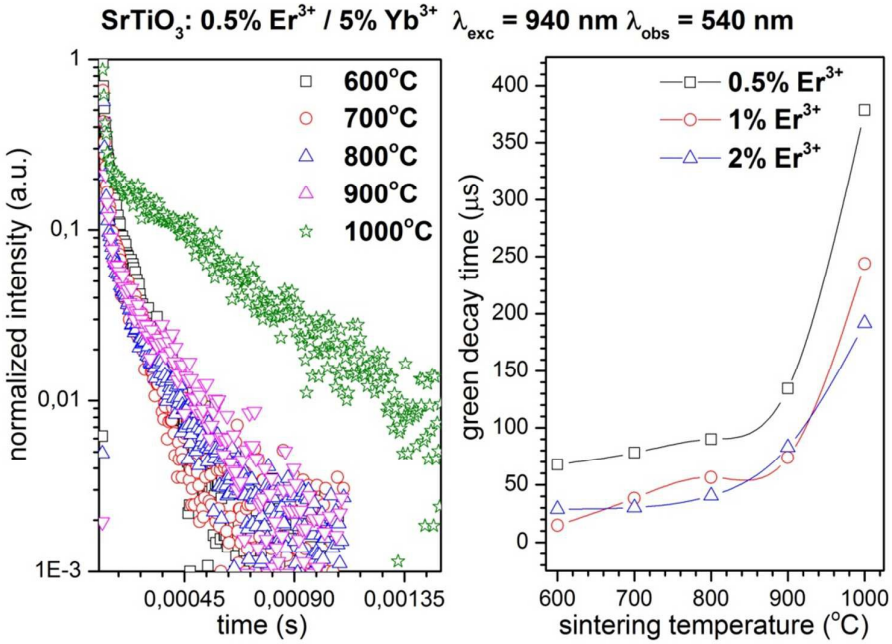

Figure 11. Luminescence decays curves of green band of the $SrTiO_3$particles doped with 0.5 mol% Er^{3+} and 5 mol% Yb^{3+} (left) as well as temperature and Er^{3+} decay times dependence (right).

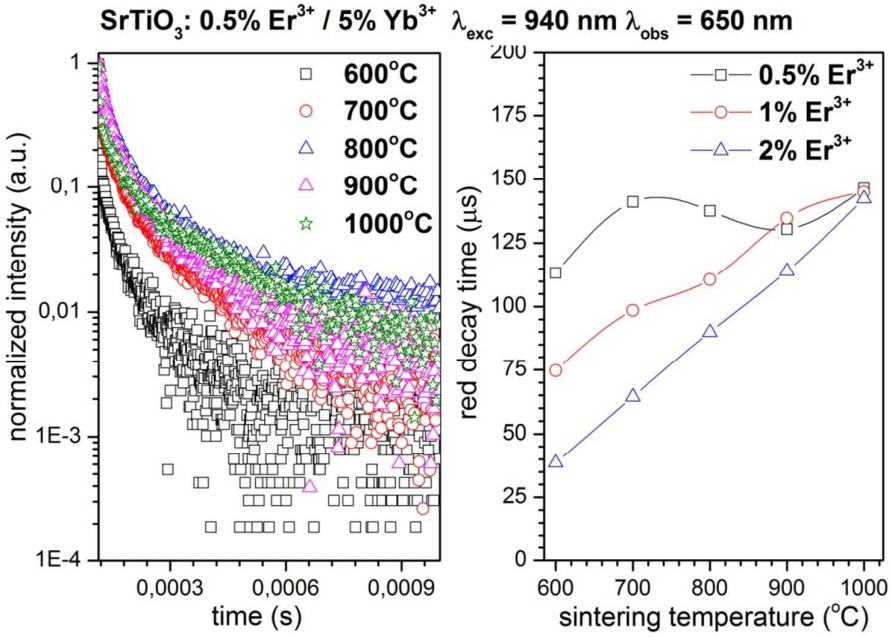

Figure 12. Luminescence decays curves of red band of the $SrTiO_3$particles doped with 0.5 mol% Er^{3+} and 5 mol% Yb^{3+} (left) as well as temperature and Er^{3+} decay times dependence (right).

The values of decay times depend strongly on the sintering temperature (particle size) and Er^{3+} ions concentration. In a classic up-converting materials or micrometer scale compounds the lifetimes are of few hundred microseconds either for green and red emission. The particle size effect is evident since increased concentration of the optically active ions is placed near particle surface leading to the quenching due to the surface defects or impurities.

Additionally, the non-exponential character of decay curves might reflect the non-homogenous distribution of dopants within particle volume as well as presence of Er^{3+} ions located at multi-sites. Increase of temperature leads to the decrease of surface atoms as well as distribution of ions within particle and therefore, decay times were increasing reaching values comparable with bulk materials. In the case of the Er^{3+} ions doping increased concentration of optically active ions results in the concentration quenching effect due to the efficient donor-donor energy transfer [49].

Cytotoxic activity of $SrTiO_3$ Er^{3+} / Yb^{3+} nanoparticles to human red blood cells

In vitro cytotoxicity assessment of the $SrTiO_3$ Er^{3+} and Yb^{3+} co-doped nanoparticles to human erythrocytes were conducted as dependence of the sample annealing temperature and Yb^{3+} ions concentration since its content would be more relevant than Er^{3+} ions. It was proved that the analyzed nanoparticles induced the cell membrane permeability and hemolysis up to concentration of 0.1 mg/ml in colloids (supplementary Figure 10s). It was found, that the $SrTiO_3$ nanoparticles affected erythrocyte sedimentation rate of the RBC in a dose-dependent manner (supplementary Figure 11s). Most likely, it might be caused by strong interactions and binding of nanoparticle aggregates to the cell membrane. The effect was visible for concentration higher than 0.1 mg/ml of nanoparticles whereas erythrocytes treated with concentration below 0.1 mg/ml settled down with the same rate as the control sample. Therefore, the $SrTiO_3$ nanoparticles doped with Er^{3+} and Yb^{3+} did not show any cytotoxic effect on the RBC up to 0.1 mg/ml.

4. Conclusions

$SrTiO_3$ nanoparticles co-doped with broad concentration range of the Er^{3+} and Yb^{3+} ions were fabricated using citric route as a function of annealing temperature 500-1000^{o}C. Formation of the amorphous phase was detected at 500^{o}C whereas crystallization into final product occurs at 600^{o}C. Further increase of annealing temperature up to 1000^{o}C resulted in narrowing of diffraction peaks (grain growth) and better product crystallinity. The mean particle size from TEM was around 30 nm for powder thermally treated at 600^{o}C whereas increase of temperature lead to the fast particle growth even above 150 nm for at 1000^{o}C. Optimization of co-dopant concentration was done in order to find balance between structural purity and satisfactory up-conversion properties. It was shown that at fixed concentration of the Yb^{3+} ions (5mol%) and increase of the Er^{3+} ions up to 2 mol% did not change structure of material for products sintered below 900^{o}C. In the case of Yb^{3+} content set at 15 mol% still solid solution of $SrTiO_3$ is kept up to 800^{o}C. Inhibitive action of Yb^{3+} ions above 20mol% on

the crystallization temperature was found. In highly concentrated samples, the phase separation was induced by annealing affecting the thermodynamic equilibrium. The multiphase materials were obtained for Yb^{3+} ions concentration higher than 10 mol% starting from 900°C. In the context of material purity the $SrTiO_3$ doped with 0.5 mol% of Er^{3+} and 5 mol% Yb^{3+} ions were optimal.

Constant increase of intensity of the green bands and decrease of red transition with increase of particle size was observed. The highest *GRR* ratio was obtained for samples not exceeding 5 mol% of Yb^{3+}. Further increase of the Yb^{3+} ions had detrimental effect on up-conversion in the $SrTiO_3$ matrix due to destabilizing action of Yb^{3+} ions on the perovskite structure. It was shown, that the role of annealing temperature relied on enhancement of up-conversion efficiency. The highest *GRR* values were obtained for the largest particles. In the case of nanoparticles higher fraction of optically active cations were located closer to the surface. Hence, non-radiative deactivation occurred due to presence of impurities, surface states, defects, ion clusters etc.

Strong power dependence of the green and red emission was found resulting in determination of temperature operating range of the $SrTiO_3$ nanoparticles as material for fast and local microscopic heating and heat release induced by the IR irradiation.

Up-conversion emission color tuning was achieved by particle size control. The color changed from white-red-yellow-green upon increase of sintering temperature inducing changes in surface-to-volume ratio and number of optically active ions in the particle surface regions. Behavior of power dependence and relatively low values of *n* showed strong contribution of non-radiative processes (CR and MPR). Non-exponential character of decay curves pointed out on non-homogenous distribution of dopants within particle volume as well as presence of Er^{3+} located at multi-sites. Increase of sintering temperature lead to the decrease of surface atoms, improvement of ions distribution and therefore, decay times of both green and red emissions reached values comparable with bulk materials.

Analyzed nanoparticles did not induce RBC cell membrane permeability and hemolysis up to particle concentration of 0.1 mg/ml. It was found, that the $SrTiO_3$ nanoparticles affect erythrocyte sedimentation rate of the RBC in a dose-dependent manner. Thus it might be concluded that $SrTiO_3$ nanoparticles doped with Er^{3+} and Yb^{3+} did not show any cytotoxic effect on the RBC up to 0.1 mg/ml.

Acknowledgements

The authors would like to thank M.Sc. Ewa Bukowska for performing XRD measurements as well as Ph.D. J. Kowalczyk for technical assistance during particle synthesis. Financial support of the National Science Centre in

course of realization of the Project 'Smart nanoparticles for bio-imaging and drug delivery' no. UMO-2011/01/D/ST5/05827 is gratefully acknowledged.

References

1 K.-M. Choi, H.-S. Kil, Y.-S. Lee, D.-Y. Lim, S.-B. Cho and B. W. Lee, *J. Lumin.*, 2011, **131**, 894–899.

2 U. Sulaeman, S. Yin and T. Sato, *Appl. Catal. B Environ.*, 2011, **105**, 206–210.

3 P. Irvin, J. Levy, J. H. Haeni and D. G. Schlom, *Appl. Phys. Lett.*, 2006, **88**, 042902.

4 L. F. da Silva, L. J. Q. Maia, M. I. B. Bernardi, J. a. Andrés and V. R. Mastelaro, *Mater. Chem. Phys.*, 2011, **125**, 168–173.

5 R. Loetzsch, a. Lübcke, I. Uschmann, E. Förster, V. Große, M. Thuerk, T. Koettig, F. Schmidl and P. Seidel, *Appl. Phys. Lett.*, 2010, **96**, 071901.

6 F. Fujishiro, T. Arakawa and T. Hashimoto, *Mater. Lett.*, 2011, **65**, 1819–1821.

7 B. Marí, K. C. Singh, P. Cembrero-Coca, I. Singh, D. Singh and S. Chand, *Displays*, 2013, **34**, 346–351.

8 M. Zalewska, B. Lipowska-Łastówka and A. M. Kłonkowski, *J. Non. Cryst. Solids*, 2010, **356**, 2070–2075.

9 F. Agnoli and M. Bettinelli, 2002, **57**, 183–187.

10 A. Maheshwari, S. B. Rai, O. Parkash and D. Kumar, *Opt. Mater. (Amst).*, 2011, **34**, 298–302.

11 F. C. D. Lemos, J. E. C. da Silva, D. M. a. Melo, M. S. C. Câmara, P. S. de Lima and C. E. J. Carneiro, *Inorg. Mater.*, 2008, **44**, 866–869.

12 H. Guo, N. Dong, M. Yin, W. Zhang, L. Lou and S. Xia, *J. Alloys Compd.*, 2006, **415**, 280–283.

13 C.-H. Quek and K. W. Leong, *Nanomaterials*, 2012, **2**, 92–112.

14 B. Va and J. S. Roma, 2003, 94–104.

15 Y. Xin, J. Jiang, K. Huo, T. Hu and P. K. Chu, **3**, 3228–3234.

16 R. J. Wiglusz, B. Pozniak, K. Zawisza and R. Pazik, *RSC Adv.*, 2015, **5**, 27610–27622.

17 E. Cenni, G. Ciapetti, D. Granchi, S. Stea, L. Savarino, a Corradini and a Di Leo, *Acta Orthop. Scand.*, 2001, **72**, 86–93.

18 D. Bao, X. Yao, N. Wakiya, K. Shinozaki and N. Mizutani, *Appl. Phys. Lett.*, 2001, **79**, 3767.

19 T. Kimijima, K. Kanie, M. Nakaya and A. Muramatsu, *Appl. Catal. B Environ.*, 2014, **144**, 462–467.

20 T. Tsumura, K. Matsuoka and M. Toyoda, *J. Mater. Sci. Technol.*, 2010, **26**, 33–38.

21 H. Cui, M. Zayat and D. Levy, *J. Non. Cryst. Solids*, 2007, **353**, 1011–1016.

22 T. Klaytae, P. Panthong and S. Thountom, *Ceram. Int.*, 2013, **39**, S405–S408.

23 Q. Zou and Z. Meng, *J. Am. Ceram. Soc.*, 1995, **78**, 58–64.

24 L. E. A. P. Klug, *X-ray Diffraction Procedure*, Wiley, New York, 1954.

25 M. Runowski, A. Ekner-grzyb, L. Mro, T. Grzyb, J. Paczesny, A. Zep and S. Lis, 2014.

26 H. M. Rietveld, *J. Appl. Crystallogr.*, 1969, **2**, 65–71.

27 S. E. . Delhez R., de Keijser T.H., Langford J.I., Louër D., Mittemeijer E.J., *Crystal Imperfection Broadening and Peak Shape in the Rietveld Method, in: The Rietveld Method,* Oxford Science, Oxford, 1993.

28 L. Lutterotti and P. Scardi, *J. Appl. Crystallogr.*, 1990, **23**, 246–252.

29.

30 C. A. R. Youed Tsur, Timothy D. Dunbar, *J. Electroceramics*, 2001, **7**, 25–34.

31 V. Palkar, P. Ayyub, S. Chattopadhyay and M. Multani, *Phys. Rev. B*, 1996, **53**, 2167–2170.

32 X. Wu, D. Wu and X. Liu, *Solid State Commun.*, 2008, **145**, 255–258.

33 B. G. Almeida, a. Pietka, P. Caldelas, J. a. Mendes and J. L. Ribeiro, *Thin Solid Films*, 2006, **513**, 275–282.

34 S. Maletic, D. Maletic, I. Petronijevic, J. Dojcilovic and D. M. Popovic, *Chinese Phys. B*, 2014, **23**, 026102.

35 S. U. Tt, 1969, **1366**.

36 M. Mączka, M. Ptak, M. Kurnatowska, L. Kępiński, P. Tomaszewski and J. Hanuza, *J. Solid State Chem.*, 2011, **184**, 2446–2457.

37 C. N. George, J. K. Thomas, R. Jose, H. P. Kumar, M. K. Suresh, V. R. Kumar, P. R. S. Wariar and J. Koshy, *J. Alloys Compd.*, 2009, **486**, 711–715.

38 V. Castano, 2001, **401**, 118–123.

39 H. Background, T. Examples, E. Discrimination, S. P. States, C. Pair, V. Fields and C. Processes, 2004.

40 K. W. Kra, D. Biner, G. Frei, H. U. Gu, M. P. Hehlen and S. R. Lu, 2004, **28**, 1244–1251.

41 J. F. Suyver, J. Grimm, K. W. Krämer and H. U. Güdel, *J. Lumin.*, 2005, **114**, 53–59.

42 J. Méndez-Ramos, P. Acosta-Mora, J. C. Ruiz-Morales and N. M. Khaidukov, *J. Alloys Compd.*, 2013, **575**, 263–267.

43 B. Zorman, M. V. Ramakrishna and R. a. Friesner, *J. Phys. Chem.*, 1995, **99**, 7649–7653.

44 T. V Gavrilović, D. J. Jovanović, V. Lojpur and M. D. Dramićanin, *Sci. Rep.*, 2014, **4**, 4209.

45 B. Dong, S. Xu, J. Sun, S. Bi, D. Li, X. Bai, Y. Wang, L. Wang and H. Song, *J. Mater. Chem.*, 2011, **21**, 6193.

46 M. Pollnau, D. Gamelin, S. Lüthi, H. Güdel and M. Hehlen, *Phys. Rev. B*, 2000, **61**, 3337–3346.

47 L. Liu, H. Jiang, Y. Chen, X. Zhang, Z. Zhang and Y. Wang, *J. Lumin.*, 2013, **143**, 423–431.

48 R. Pazik, D. Hreniak, W. Strek, a. Speghini and M. Bettinelli, *Opt. Mater. (Amst).*, 2006, **28**, 1284–1288.

49 L. G. Van Uitert, R. C. Linares, R. R. Soden and a. a. Ballman, *J. Chem. Phys.*, 1962, **36**, 702.

Supplementary Information

Functional up-converting $SrTiO_3:Er^{3+}/Yb^{3+}$ nanoparticles, structural features, particle size colour tuning and *in vitro* RBC cytotoxicity

R. Pazik [1*], M. Mączka[1], M. Malecka[1], L. Marciniak[1], L. Mrowczynska[2], A. Ekner-Grzyb[3], and R.J. Wiglusz[1]

[1]*Institute of Low Temperature and Structure Research, PAS, Okólna 2, 50-422 Wrocław, Poland*

[2]*Adam Mickiewicz University, Faculty of Biology, Department of Cell Biology, Umultowska 89, 61-614 Poznań, Poland*

[3]*Adam Mickiewicz University, Faculty of Biology, Department of Behavioural Ecology, Umultowska 89, 61-614 Poznań, Poland*

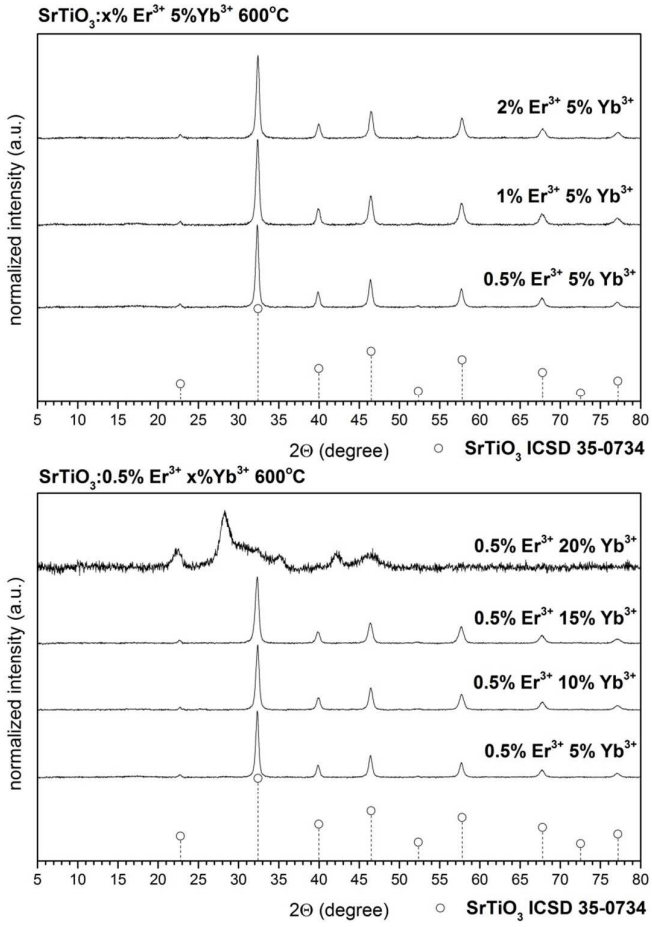

Fig. 1s. Effect of Er^{3+} (upper) and Yb^{3+} (bottom) concentration of crystal structure of the $SrTiO_3$ heated at 600°C.

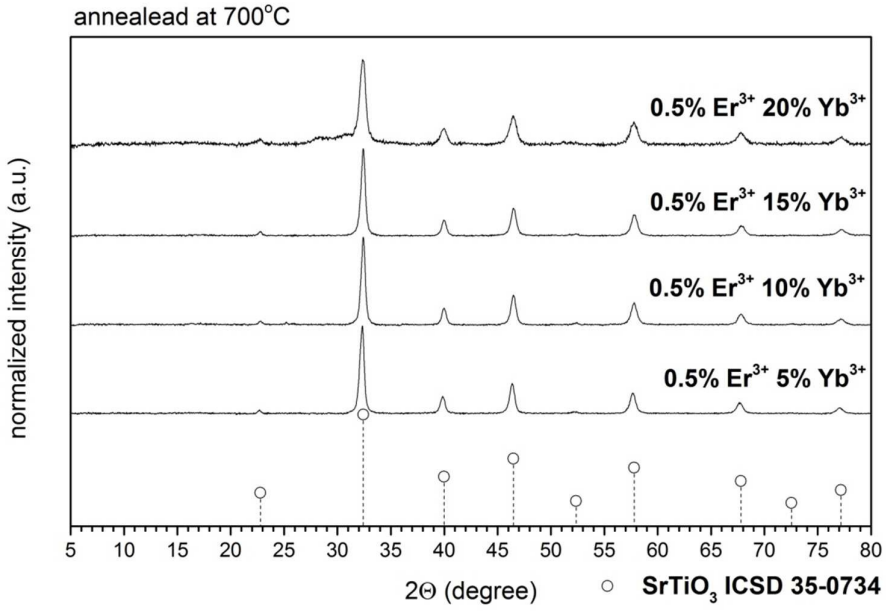

Fig. 2s. Compare with sample containing 20 mol% of Yb^{3+} heat treated at 600°C with 20 mol% Yb^{3+} sample at 700°C.

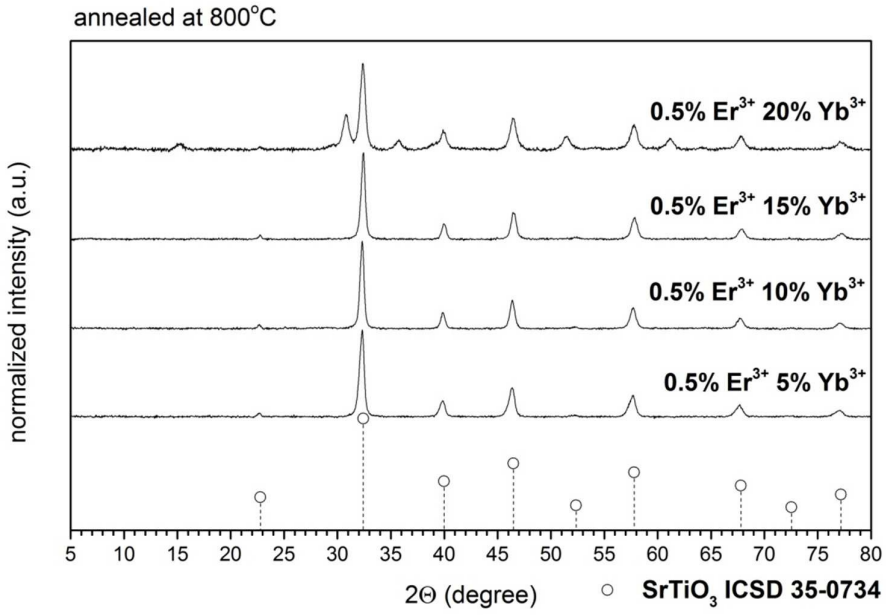

Fig. 3s. Note phase separation of the $SrTiO_3$ above 20 mol% of Yb^{3+} at 800°C.

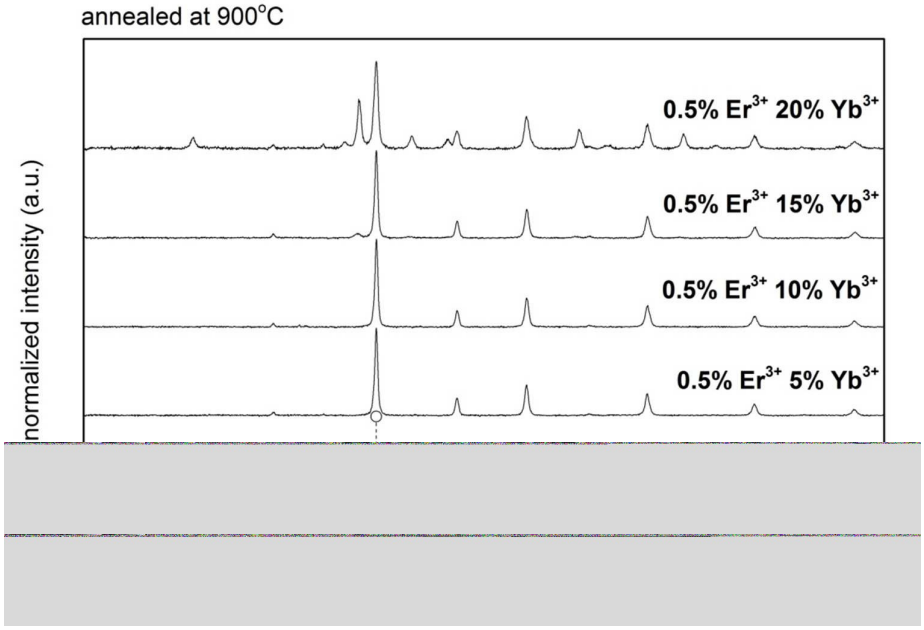

Fig. 4s. Note phase separation of the $SrTiO_3$ with different content of Yb^{3+} above 15 mol% at 900°C.

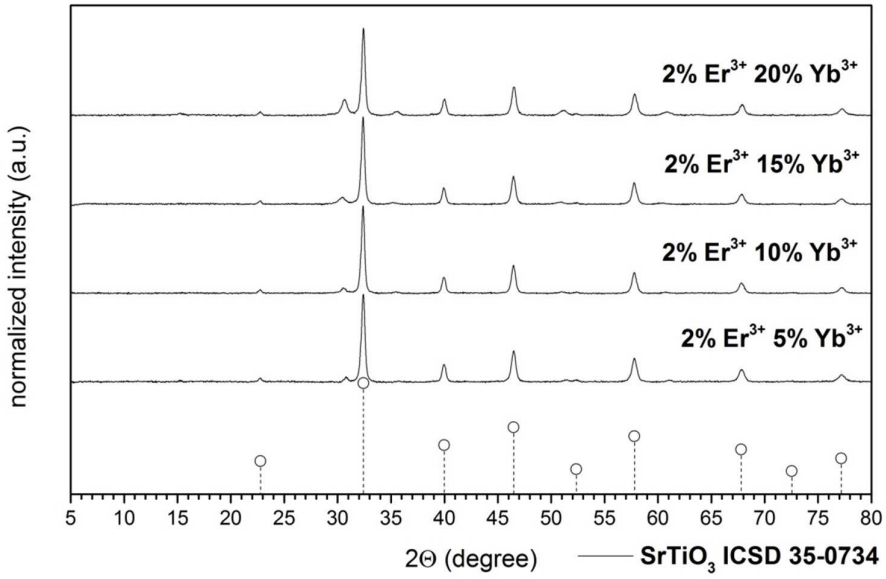

Fig. 5s. Note phase separation of the $SrTiO_3$ with 2 mol% of Er^{3+} and different content of Yb^{3+} samples heated at 900°C.

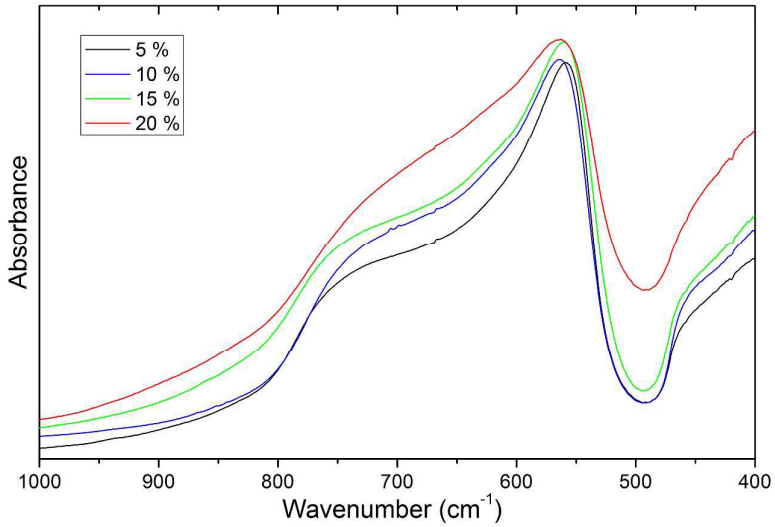

Fig. 6s. Mid-IR spectra of $SrTiO_3$ doped with 5, 10, 15 and 20 % of Yb^{3+} and 0.5 % of Er^{3+} annealed at 800 °C.

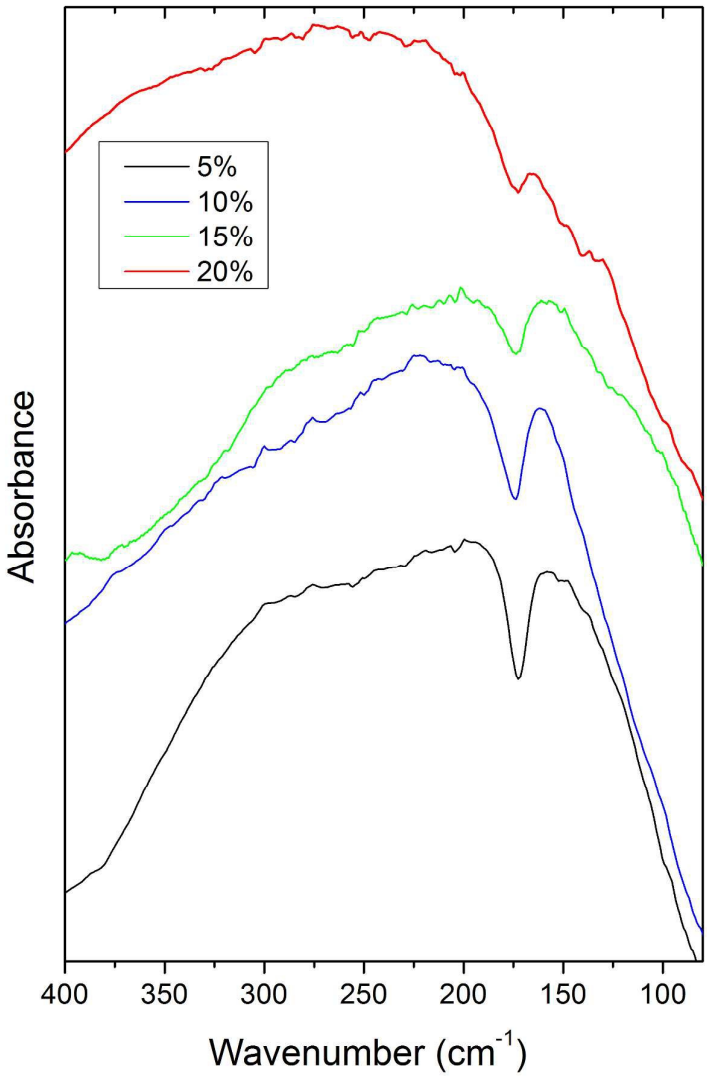

Fig. 7s. Far-IR spectra of $SrTiO_3$ doped with 5, 10, 15 and 20 % of Yb^{3+} and 0.5 % of Er^{3+} annealed at 800 °C.

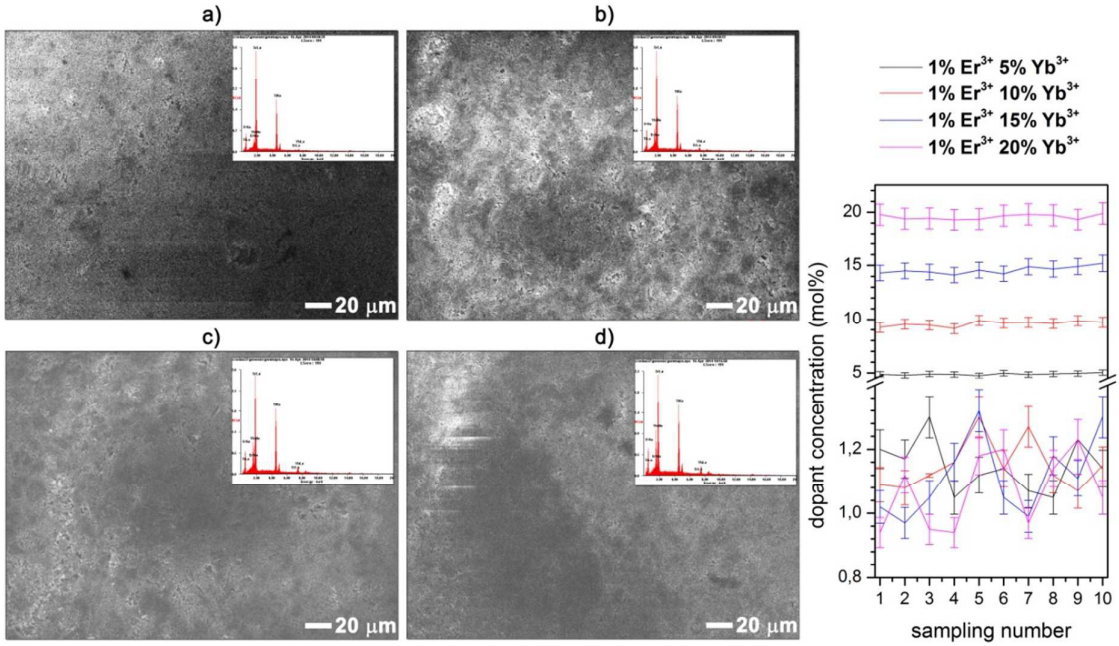

Fig. 8s. SEM-EDX analysis of the $SrTiO_3$ 1% Er^{3+} / x% Yb^{3+} nanoparticles sintered at 600°C.

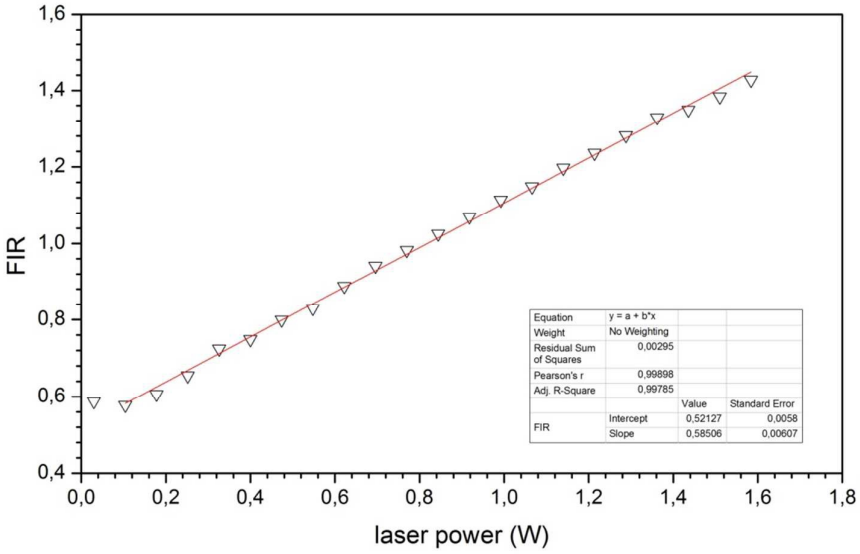

Fig. 9s. Calibration curve FIR vs. pump power.

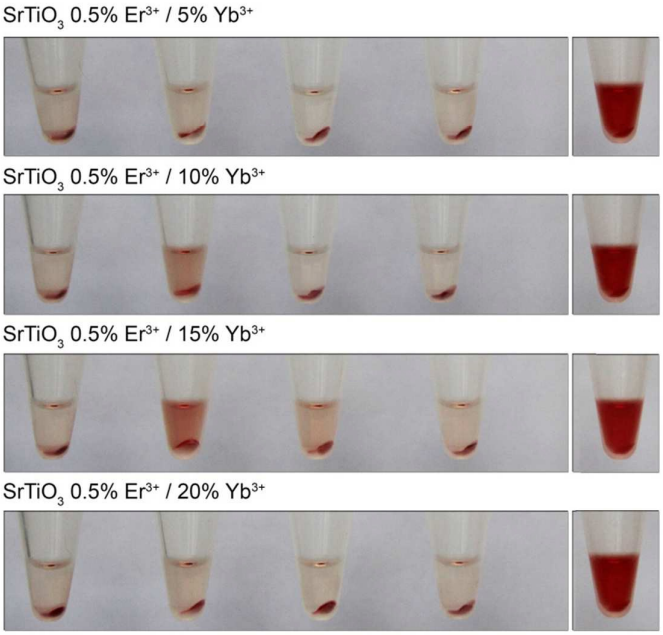

Fig. 10s. Hemolysis assay on human erythrocyte cells loaded with the $SrTiO_3$ 0.5% Er^{3+} / x% Yb^{3+} nanoparticles annealed at 600°C (from left side: negative control (PBS), 1 mg/ml, 0.1 mg/ml, 0.01 mg/ml, positive control (100% hemolysis, distilled water).

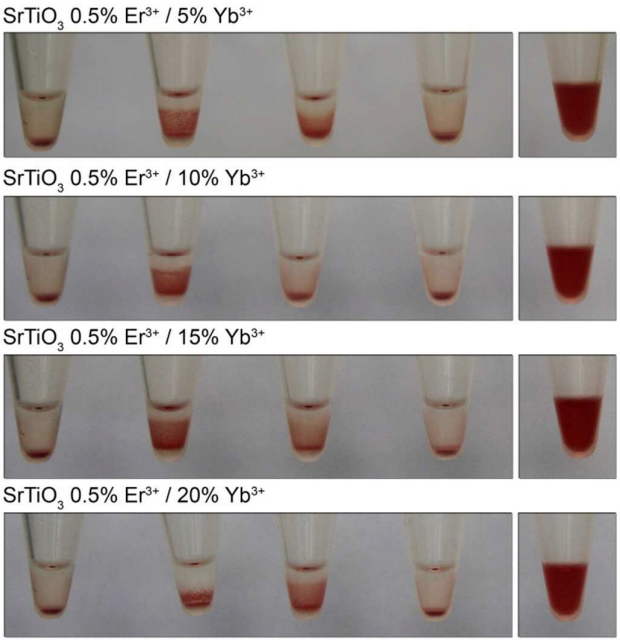

Fig. 11s. ESR of human erythrocyte cells loaded with the $SrTiO_3$ 0.5% Er^{3+} / x% Yb^{3+} nanoparticles annealed at 600°C (from left side: negative control (PBS), 1 mg/ml, 0.1 mg/ml, 0.01 mg/ml, positive control (100% hemolysis, distilled water).